Lamb wave mode decomposition using concentric ring and circular piezoelectric transducers

Chul Min Yeum [a], Hoon Sohn [a,*], Jeong Beom Ihn [b]

[a] The Department of Civil and Environmental Engineering, Korea Advanced Institute of Science and Technology, Daejeon 305-701, South Korea
[b] Boeing Research & Technology, 9725 East Marginal Way South, Mail Code 42-25 Seattle, WA 98108, United States

ARTICLE INFO

ABSTRACT

Lamb waves using surface-bonded piezoelectric transducers (PZTs) have been widely used for nondestructive testing (NDT). However, the identification of individual Lamb wave modes and the subsequent data interpretation are often difficult due to the dispersive and multimodal natures of Lamb waves. To tackle the problem, a Lamb wave mode decomposition technique using concentric ring and circular PZTs is proposed. Its advantages over the conventional approaches are that (1) PZTs need to be placed only a single surface of a specimen and (2) mode decomposition can be performed at any desired frequency without changing the PZT size and/or spacing configuration. The proposed mode decomposition technique is formulated by solving 3D Lamb wave propagation equations considering the PZT size and shape, and this technique requires a specially designed dual PZT composed of concentric ring and circular PZTs. The effectiveness of the proposed technique for the Lamb wave mode decomposition is investigated through numerical simulation and experimental tests performed on an aluminum plate.

© 2011 Elsevier B.V. All rights reserved.

1. Introduction

Lamb waves have gained a great deal of attention for structural health monitoring (SHM) and nondestructive testing (NDT) of plate-like structures [1–4]. Lamb waves are mechanical waves whose wavelength is in the same order of magnitude as the thickness of the plate. One of the main advantages of Lamb waves is that they can travel considerable distances with little attenuation, allowing the inspection of large areas. However, the analysis and interpretation of Lamb waves can be complicated due to their dispersive and multimodal natures. The various frequency components of Lamb waves travel at different speeds, causing the shape distortion of wave packets. Furthermore, there exit multiple modes, at least two modes, at any specific driving frequency, making subsequent signal interpretation challenging.

To ease the analysis and interpretation of Lamb waves, selective Lamb wave generation and sensing have been investigated. Examples of the selective Lamb wave generation and sensing techniques include (1) angle wedge tuning using contact and non-contact type wedge transducers [11,12], (2) wavelength-matched linear arrays, using comb transducers [13,14], and (3) point source point receiver (PS-PR) using Hertzian contacts and non-contact laser beams [15,16]. However, these conventional techniques have drawbacks and limitations. Some of the conventional transducers may be too heavy and bulky for online monitoring of structures such as airplanes and have directionality for selective Lamb wave mode generation and sensing. Furthermore, due to their relatively high cost, they are not suitable for deployment to large-scale structures. Lastly, some parameters of the transducer such as the incidence angle of the wedge transducer or the element spacing of the comb transducer need to be manually adjusted for selective Lamb wave excitation and sensing at a different frequency.

* Corresponding author. Tel.: +82 42 350 3625; fax: +82 42 350 3610.
E-mail addresses: chulminy@gmail.com (C.M. Yeum), hoonsohn@kaist.ac.kr (H. Sohn), Jeong-Beom.Ihn@boeing.com (J.B. Ihn).

Recently, embedded or surfaced-bonded PZTs are used to overcome some of the conventional transducers' drawbacks. In particular, the use of piezoelectric wafer transducers (hereafter, PZTs) is becoming popular for online SHM due to their light weight, unobtrusive nature, and low cost [5–10]. Mode isolation techniques using PZTs include (1) placement of collocated PZTs on both surfaces of a specimen [17], (2) an array of PZTs with time delays [18], and (3) tuning of the driving frequency and/or the PZT size for a specific mode excitation and sensing [19,20]. For the collocated PZT technique, a specific Lamb mode can be excited or measured using the polarization characteristics of the PZT. However, access to both surfaces of a structure can be limited, and precise placement of collocated PZTs can be a challenging task. The PZT array technique can also selectively generate a desired Lamb wave mode by tuning the spacing of the PZT array and applying time delays to the PZT array. However, the PZT array requires a multi-channel data acquisition system and precise control of prescribed time delay profiles. For the tuning technique, the isolation of a single Lamb mode is possible only at a specific frequency where the target mode is predominant or by tuning the PZT size to the half of the target mode's wavelength. That is, the mode selection is possible only at a specific frequency and for a fixed PZT size.

In this study, a new Lamb wave mode decomposition technique is proposed so that fundamental symmetric (S_0) and anti-symmetric (A_0) modes can be decoupled at an arbitrary driving frequency without adjustment of the PZT size. First, the response models of circular and ring shape PZTs are derived, and the proposed mode decomposition technique is formulated based on the response model of a dual PZT, that is composed of concentric ring and circular PZTs. Then, numerical simulation and experimental tests are executed to investigate the feasibility of the proposed technique. The advantages of the proposed technique are that (1) PZTs need to be placed only a single surface of the structure, (2) mode decomposition can be performed at any desired frequency without physical adjustment of the PZT size and/or spacing, (3) both S_0 and A_0 modes can be simultaneously decoupled and identified at any driving frequency, and (4) a circular design of the dual PZT allows omni-directional Lamb wave decomposition.

2. Theoretical formulation

The proposed mode decomposition technique decouples fundamental Lamb wave (S_0 and A_0) modes from measured signals without PZT size adjustment or frequency tuning. The basic premise behind the proposed technique is that the amplitudes of the S_0 and A_0 modes change at "different" rates, as the sizes of the excitation and sensing PZTs vary. Based on this premise, a new "dual" PZT composed of co-centered circular and ring PZTs is designed and the mode decomposition is realized by manipulating multiple signals measured by activating different parts of the dual PZTs for excitation and sensing. Because the proposed technique can decompose only the S_0 and A_0 modes, the applicable frequency range is limited below the cutoff frequencies of the S_1 or A_1 modes.

This section is organized as follows. First, an analytical solution of the Lamb wave propagation modeling using 3D circular PZT actuation and sensing is derived. Note that although the Lamb wave propagation models for 2D and 3D rectangular PZTs, and 3D circular PZT excitation and 3D rectangular PZT sensing have been previously developed [5,21], the Lamb wave propagation model using the full 3D circular PZTs is first developed in this study. Second, a newly designed dual PZT is introduced, and a Lamb wave decomposition technique using the dual PZT is developed. Third, a procedure to estimate the normalized scaling factors, necessary for the proposed decomposition technique, from measured signals is described. Finally, the performance and limitations of the proposed decomposition technique at different situations are discussed.

2.1. Analytical solution of the Lamb wave response at a circular PZT

First, the analytical displacement response at an arbitrary distance from an exciting circular PZT is presented. Fig. 1 presents an isotropic plate with one pair of exciting and sensing circular PZTs bonded on a single surface. Assuming that the exciting circular PZT is located at the origin of a polar coordinate system ($r = 0$) and it produces axisymmetric circular waves, the circumferential displacement (u_θ) and the derivative with respect to θ ($\partial/\partial\theta$) become zero. When the excitation PZT is assumed to be perfectly
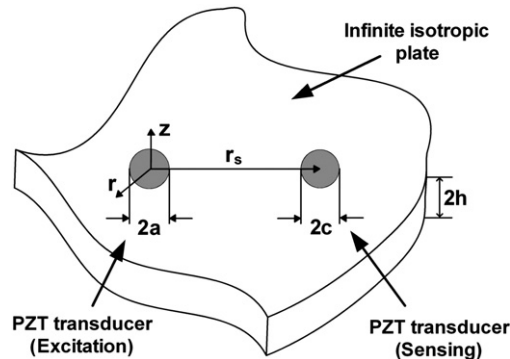

Fig. 1. Two circular PZTs bonded on a surface of an infinite isotropic plate.

bonded to the plate, the excitation can be modeled using the 'pin-force model' that only produces surface shear stress around its circumference boundary. Then, the shear stress at a specific excitation frequency ω becomes $\tau_{zr} = \tau_0 \delta(r-a) \cdot e^{i\varpi t}$. Here, δ is the Dirac delta function and τ_0 is the amplitude of the generated shear stress. The radial displacement (u_r) at a distance of r from the exciting circular PZT becomes [5]:

$$u_r(r, z = h) = -\pi i \frac{\tau_0 a}{\mu} e^{i\omega t} \cdot \left[\sum_{\xi^S} J_1(\xi^S a) \frac{N_S(\xi^S)}{D'_S(\xi^S)} H_1^{(2)}(\xi^S r) + \sum_{\xi^A} J_1(\xi^A a) \frac{N_A(\xi^A)}{D'_A(\xi^A)} H_1^{(2)}(\xi^A r) \right] \tag{1}$$

where

$$\alpha^2 = \frac{\omega^2}{c_L^2} - \xi^2, \beta^2 = \frac{\omega^2}{c_T^2} - \xi^2, c_L = \sqrt{\frac{\lambda + 2\mu}{\rho}}, c_T = \sqrt{\frac{\mu}{\rho}},$$

$$N_S = \xi\beta(\xi^2 + \beta^2)\cos\alpha h \cos\beta h, \; D_S = (\xi^2 - \beta^2)^2 \cos\alpha h \sin\beta h + 4\xi^2\alpha\beta \sin\alpha h \cos\beta h,$$

$$N_A = \xi\beta(\xi^2 + \beta^2)\sin\alpha h \sin\beta h, \; D_A = (\xi^2 - \beta^2)^2 \sin\alpha h \cos\beta h + 4\xi^2\alpha\beta \cos\alpha h \sin\beta h.$$

λ and μ are the Lame constants for the plate material, and ρ is the material density of the plate. The superscripts or subscripts S and A denote the symmetric and antisymmetric Lamb modes, respectively. The wavenumber ξ of a specific mode at a given ω is obtained by solving the Rayleigh–Lamb equation of an isotropic plate [5]. $J_1()$ is the Bessel function of the first kind of order 1, and $H_1^{(2)}()$ is the Hankel function of order 1 of the second type.

Next, the voltage response of a circular sensing PZT is calculated by integrating the strain field over the entire area of the sensing PZT and considering the piezoelectricity of the sensing PZT. The deformation of the sensing PZT creates charge (Q_P), and the output voltage (V) at the sensing PZT is obtained by dividing the charge by the PZT capacitance value (C_P):

$$V(t) = \frac{Q_P}{C_P} = \frac{E_s h_s g_{31}}{A} \int_A \varepsilon_{kk} dA \tag{2}$$

where E_s, h_s and A are Young's modulus, thickness, and surface area of the sensing PZT, respectively. g_{31} is the xz-directional piezoelectric voltage constant and ε_{kk} is the sum of the in-plane extensional surface strains. When the shape of the sensing PZT is circular, the area integral in Eq. (2) becomes

$$V(t) = \frac{E_s h_s g_{31}}{A} \iint_A (\varepsilon_{rr} + \varepsilon_{\theta\theta}) r dr d\theta = \frac{E_s h_s g_{31}}{A} \iint_A \left(\frac{du_r}{dr} + \frac{u_r}{r} \right) r dr d\theta. \tag{3}$$

Because of the axisymmetric nature of the wave propagations, all u_θ and $\partial/\partial\theta$ terms vanish and only ε_{rr} and $\varepsilon_{\theta\theta}$ terms remain. By substituting the radial displacement in Eq. (1) into Eq. (3), the output voltage at the sensing PZT becomes

$$V(t) = -i\frac{\tau_0 E_s h_s g_{31} a}{\mu c^2} e^{i\omega t} \left[\begin{array}{l} \sum_{\xi^S} J_1(\xi^S a) \frac{N_S(\xi^S)}{D'_S(\xi^S)} \iint_A \xi^S r H_0^{(2)}(\xi^S r) dr d\theta \\ + \sum_{\xi^A} J_1(\xi^A a) \frac{N_A(\xi^A)}{D'_A(\xi^A)} \iint_A \xi^A r H_0^{(2)}(\xi^A r) dr d\theta \end{array} \right] \tag{4}$$

where $H_0^{(2)}()$ is the complex Hankel function of order 0 of the second type.

Eq. (4) can be further simplified into Eq. (5) by assuming that (1) the distance between the excitation and sensing PZTs is much longer compared to the size of the sensing PZT and (2) the complex Hankel function shows an asymptotic behavior after four or five cycles of the wavelength of the excited mode [21]. The detailed derivation of Eq. (5) is provided in Appendix A.

$$V(t) = -i\frac{2\tau_0 E_s h_s g_{31} a}{\mu c} \sqrt{\frac{2\pi}{r_s}} \left[\begin{array}{l} \frac{1}{\sqrt{\xi^{S_0}}} J_1(\xi^{S_0} a) J_1(\xi^{S_0} c) \frac{N_S(\xi^{S_0})}{D'_S(\xi^{S_0})} e^{i\left(\omega t - \frac{\pi}{4} + \xi^{S_0} r_s\right)} \\ + \frac{1}{\sqrt{\xi^{A_0}}} J_1(\xi^{A_0} a) J_1(\xi^{A_0} c) \frac{N_S(\xi^{A_0})}{D'_S(\xi^{A_0})} e^{i\left(\omega t - \frac{\pi}{4} + \xi^{A_0} r_s\right)} \end{array} \right] \tag{5}$$

Eq. (5) shows that given the driving frequency and the corresponding wavenumber of each mode, the arrival times of the S_0 and A_0 modes are controlled only by the distance between the sensing and excitation PZTs (r_s) and not affected by their sizes. On

the other hand, the amplitudes of the S_0 and A_0 modes are functions of the excitation and sensing PZT sizes (a and c) as well as the geometrical attenuation due to 2D energy dissipation ($1/\sqrt{r_s}$). Thus, the terms in Eq. (5) can be grouped into two categories: one controlled by r_S and the other controlled by a and c:

$$V(t) = C^{S_0}(t, r_s) S^{S_0}(a, c) + C^{A_0}(t, r_s) S^{A_0}(a, c) \tag{6}$$

where

$$C^{S_0}(t, r_s) = -i \frac{2\sqrt{2\pi}\tau_0 E_s h_s g_{31}}{\mu \sqrt{\xi^{S_0} r_s}} \frac{N_S\left(\xi^{S_0}\right)}{D'_S\left(\xi^{S_0}\right)} e^{i\left(\omega t - \frac{\pi}{4} + \xi^{S_0} r_s\right)}$$

$$S^{S_0}(a, c) = \frac{a}{c} J_1\left(\xi^{S_0} a\right) J_1\left(\xi^{S_0} c\right).$$

$C^{A_0}(t, r_S)$ and $S^{A_0}(a, c)$ are defined in a similar fashion.

Note that, because the S_0 and A_0 modes have different wavenumbers, these two modes have different amplitudes for the same excitation and sensing PZT sizes. Furthermore, their amplitudes change at different rates as the sizes of the actuator and sensor vary.

Hypothetically assuming that all parameters are fixed except the actuator and/or the sensor sizes, the multiple response signals can be measured by varying the actuator and the sensor sizes. The values of $S^{S_0}(a, c)$ and $S^{A_0}(a, c)$ corresponding to varying actuator and sensor sizes can be analytically computed once the wavenumbers of the S_0 and A_0 modes are known. Here, the amplitudes of the S_0 and A_0 modes change at "different" rates, as the sizes of the actuator and sensor vary. Then, the common factors $C^{S_0}(t, r_S)$ and $C^{A_0}(t, r_S)$, which are independent of actuator and sensor sizes, can be estimated from multiple combinations of the response signals $S^{S_0}(a, c)$ and $S^{A_0}(a, c)$. The main challenge in this approach is to vary only the sizes of the actuator and sensor without changing the other parameters in Eq. (6) including r_S. This problem is addressed by designing a new dual PZT configuration described below.

2.2. Description of a dual PZT

Before describing the proposed decomposition technique, the configuration of a dual PZT is introduced [6,24]. Fig. 2(a) illustrates the schematic drawing of the dual PZT. The dual PZT consists of concentric ring and circular PZTs. These two PZT components can be activated independently or simultaneously for Lamb wave excitation and sensing.

By activating different parts of the excitation and sensing dual PZTs, nine different response signals can be obtained: V_{ij}, i and $j = 1, 2$ and 3. Here, i and j denote the different part(s) of the dual PZT activated for excitation and sensing. 1, 2 and 3 represent the entire, ring and circular parts of the dual PZT, respectively. For example, V_{13} in Fig. 2(b) represents the response signal measured by the circular part of the sensing dual PZT when both the ring and the circular parts of the excitation dual PZT are actuated. V_{32} is defined in a similar manner. The darker area(s) in Fig. 2(b) show(s) the PZT part(s) activated for Lamb wave excitation or sensing.

2.3. Formulation of a decomposition technique

Now using dual PZTs, multiple response signals can be obtained: V_{ij}, i and $j = 1, 2$ and 3. The theoretical response models for V_{ij} can be easily obtained from Eq. (6) by slightly modifying the equation when the ring part of the dual PZT is used either for excitation or sensing. For example, the response model of a ring PZT sensor can be obtained by integrating the surface strain over the ring PZT area. This response model of the ring PZT can be equivalently obtained by subtracting the strain over a circular PZT,
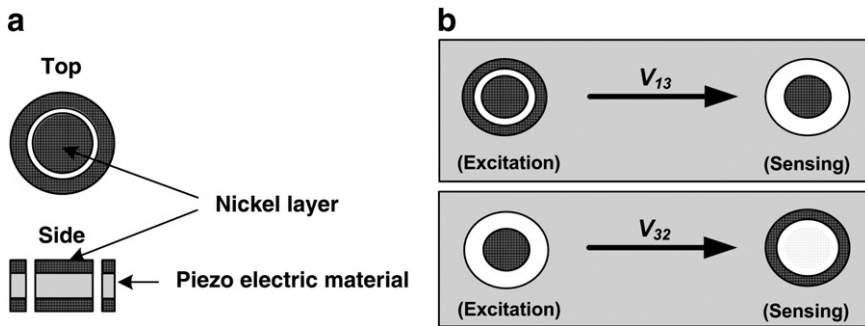

Fig. 2. A schematic drawing of the dual PZT and examples of signals obtained by the dual PZTs: (a) the configuration of the dual PZT composed of co-centered ring and circular PZTs (b) V_{13} denotes a response measured by the inner circular part of the sensing PZT when both the outer ring and the inner circular parts of the excitation PZT are activated. Similarly, V_{32} is measured by the ring part of the sensing PZT when the circular part of the excitation PZT is actuated. (Here, the subscripts, 1, 2 and 3 denote the entire dual PZT, the outer ring PZT and the inner circular PZT, respectively.) The darker area of the dual PZT represents the PZT component(s) activated either for excitation or sensing.

where its radius is the same as the inner radius of the ring PZT, from the strain over another circular PZT with its radius equal to the outer radius of the ring PZT. The derivation of these response models is detailed in Appendix B. From Appendix B, the response models for V_{ij} are obtained as follows.

$$\mathbf{V} = \mathbf{SC} \tag{7}$$

where $\mathbf{V} = \begin{bmatrix} V_{11} \\ V_{12} \\ \vdots \\ V_{33} \end{bmatrix}$, $\mathbf{S} = \begin{bmatrix} S_{11} & A_{11} \\ S_{12} & A_{12} \\ \vdots & \vdots \\ S_{33} & A_{33} \end{bmatrix}$, $\mathbf{C} = \begin{bmatrix} C^{S_0}(t, r_s) \\ C^{A_0}(t, r_s) \end{bmatrix}$

S_{ij} and A_{ij} are defined as the scaling factors similar to $S^{S_0}(a,c)$ and $S^{A_0}(a,c)$ in Eq. (6), and they depend only on the size of the PZT used. For example, S_{13} corresponds to the scaling factor when the entire dual PZT is activated for excitation and only the inner circular PZT is used for sensing.

The procedures of the proposed mode decomposition can be summarized as follows.

(1) A total of nine V_{ij} are obtained by activating different parts (the outer ring, inner circle or both) of the excitation and sensing dual PZTs

(2) For the given sizes of the dual PZTs activated for excitation and sensing, the corresponding scaling factors can be analytically or experimentally computed. The detailed procedure for the estimation of the scaling factor matrix $\mathbf{S}$ is described in the following section.

(3) The matrix $\mathbf{C}$ in Eq. (7) can be estimated by taking the pseudo-inverse of the scaling factor matrix $\mathbf{S}$ and premultiplying it to the matrix $\mathbf{V}$. Because Eq. (7) is an over-determined system, the estimated $C^{S_0}(t, r_S)$ and $C^{A_0}(t, r_S)$ are the optimal solution that minimizes the least squares errors.

(4) Finally, either the S_0 or A_0 mode in any measured signal can be decomposed and isolated. For example, the contribution of the S_0 mode in V_{13} can be obtained as $S_{13} \times C^{S_0}(t, r_S)$.

2.4. Estimation of the scaling factors from measured signals

The success of the proposed technique relies on the precise estimate of the scaling factor matrix $\mathbf{S}$ in Eq. (7). Here, the scaling factor matrix can be analytically estimated similar to the computation of a Lamb wave tuning curve, which is the amplitude plots of symmetric and antisymmetric Lamb wave modes as a function of the driving frequency. However, a theoretical Lamb wave tuning curve obtained from the analytical Lamb wave propagation model does not necessarily match well with the experimental ones, because (1) the PZT is not fully coupled with the host structure due to bonding layer, (2) consequently, the effective PZT size becomes less than the physical PZT size, and (3) material properties of the structure continuously vary due to temperature and external loading [22].

Alternatively, the scaling factors, more precisely the normalized scaling factors which will be introduced later, can be estimated solely from the measured response signals. Note that S_{ij} cannot be directly estimated from the measured V_{ij}. However, the amplitude of the S_0 mode $S_{ij} \times C^{S_0}(t, r_S)$ in any V_{ij} can be easily estimated, and it can be shown that the ratio of the signed S_0 mode amplitude in V_{ij} to that in V_{11} is $(S_{ij} \times C^{S_0}(t, r_S))/(S_{11} \times C^{S_0}(t, r_S)) = S_{ij}/S_{11}$. Therefore, the normalized scaling factors for the S_0 mode, defined as $\tilde{S}_{ij} = S_{ij} / S_{11}$, can be readily obtained from the measured signals by computing the signed amplitude ratio of the S_0 mode in V_{ij} to that in V_{11}. Similarly, the normalized scaling factors for the A_0 mode can be defined as $\tilde{A}_{ij} = A_{ij}/A_{11}$ and obtained from V_{ij}. Now, Eq. (7) can be rearranged as follows:

$$\begin{bmatrix} V_{11} \\ V_{12} \\ \vdots \\ V_{33} \end{bmatrix} = \begin{bmatrix} \tilde{S}_{11} & \tilde{A}_{11} \\ \tilde{S}_{12} & \tilde{A}_{12} \\ \vdots & \vdots \\ \tilde{S}_{33} & \tilde{A}_{33} \end{bmatrix} \begin{bmatrix} S_{11} C^{S_0}(t, r_s) \\ A_{11} C^{A_0}(t, r_s) \end{bmatrix} \tag{8}$$

where $\tilde{S}_{ij} = S_{ij} / S_{11}$, $\tilde{A}_{ij} = A_{ij}/A_{11}$.

2.5. Discussions on the performance and limitations

In this subsection, the performance and limitations of the proposed technique are discussed for several representative cases.

2.5.1. Decomposition of the overlapped S_0 and A_0 modes

The requirement in Eq. (8) is that the first arriving S_0 and A_0 modes are well separated in the time domain so that their signed amplitudes can be easily estimated. However, when the distance between the excitation and sensing PZTs is too short or there are multiple reflection paths, the estimation of the signed amplitudes of the first arriving S_0 and A_0 modes can be challenging. This problem can be addressed by placing a pair of excitation and sensing PZTs with a longer spacing so that the first arrivals of the S_0 and A_0 modes can be well separated and the normalized scaling factors can be estimated from this longer path. Note that because

the scaling factors as well as the normalized scaling factors are only functions of the wavenumbers and sizes of the actuator and sensor PZTs, they are independent of the spacing between the excitation and sensing PZTs. Therefore, the normalized scaling factors estimated from a single long path can be used for the mode decomposition in all the other paths with varying path lengths as long as they use the same sizes of the dual PZTs.

2.5.2. Conditioned matrix inversion

In general, well-conditioned matrix inversion in Eq. (8) can be achieved when there are large differences (1) between S_{ij} and A_{ij} (between scaling factors of the S_0 and A_0 modes) and (2) among S_{ij} or A_{ij} (among scaling factors within each mode). The difference between S_{ij} and A_{ij} can be increased by using a high frequency excitation because the scaling factor is a function of wavenumbers and the difference between the wavenumbers of the S_0 and A_0 modes rises at a high frequency. The amplified difference among S_{ij} (or A_{ij}) can be achieved by increasing the size discrepancy between the ring and the circular PZTs because the scaling factor is also a function of the PZT size.

2.5.3. Spreading error

When a toneburst excitation is used in real applications, large size difference between the ring and circular PZTs should be traded-off because the size difference between the ring and the circular PZTs can also increase the decomposition error due to the spreading of the decomposed individual mode in the time domain, which will be referred to as the "spreading error" hereafter. Theoretically, when a toneburst excitation with a limited time duration is applied, the time duration of a response signal depends on the actual PZT size: the larger the sensing PZT is, the more spread out the time response is. Note that $C^{S_0}(t, r_S)$ (or $C^{A_0}(t, r_S)$) in Eq. (6), in theory, has a steady-state harmonic response, but its actual time duration varies depending on the sensing PZT size when a toneburst excitation is used. That is, this spreading error results from the use of a toneburst signal although Eq. (6), which is formulated for a steady-state harmonic excitation, should not produce such spreading error. This spreading error can be reduced by using the over-determined system in Eq. (8) as examined by the numerical simulation in the next section.

3. Numerical simulation

Numerical simulation is performed in this section to further examine the performance of the proposed technique. Note that, although the theoretical equation in Eq. (6) is derived assuming a harmonic excitation with a single frequency, a narrowband toneburst input is employed for actual experiments. The use of this transient narrowband excitation rather than the steady-state harmonic excitation produces the previously mentioned spreading error. The presented FEM simulation is necessary to examine how the use of a narrowband toneburst signal and solving an over-determined system affect the proposed mode decomposition performance and the spread error.

3.1. Simulation setup

A commercially available finite element analysis (FEA) program (MSC/NASTRAN) and a pre- and post-processor (PATRAN) were used for the simulation. For the numerical simulation, a 3D aluminum plate of 200 mm × 400 mm × 3 mm was simulated as shown in Fig. 3. The PZT is assumed to be perfectly bonded to the structure and no PZT damping is considered. The input force exerted by the excitation PZT is modeled as 'pin-forces' applied along equally spaced multiple points of its circumference boundary [5]. The corresponding output response is computed by integrating the strain over the sensing PZT that is meshed on the structure. Two dual PZTs were modeled on the top surface of the plate, and the third dual PZT was modeled on the other side of the plate. PZT A and PZT C are located at an identical position but on the opposite sides.

The driving frequency was selected to be 180 kHz so that only the S_0 and A_0 modes were generated and sensed. The maximum mesh size was 1 mm × 1 mm × 1 mm, and the sampling rate of 5 ms/s was chosen to be sufficiently high to capture the smallest traveling wavelength. Rayleigh damping coefficients for the plate model were set to 10^{-4} for a mass damping coefficient and 0 for a stiffness damping coefficient, respectively.
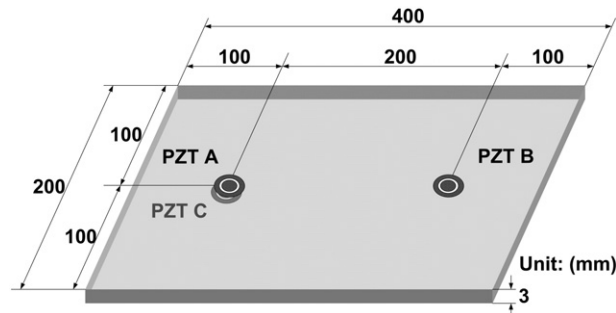

Fig. 3. The dimension and configuration of the plate structure with the dual PZTs used for numerical simulation: PZT C is placed at the same position of PZT A but on the other side of the plate.
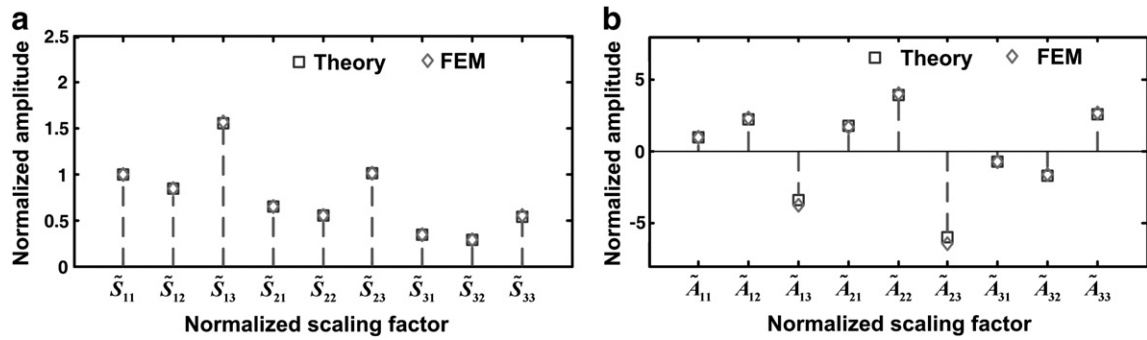
Fig. 4. Comparison of the normalized scaling factors, $\tilde{S}_{ij}$ and $\tilde{A}_{ij}$, obtained from numerical simulation and theoretical solutions: the normalized scaling factors (a) for the S_0 mode and (b) for the A_0 mode. (The rectangle and diamond indicate the theoretical and numerical normalized scaling factors, respectively.)

3.2. Simulation results

First, Fig. 4 compares the normalized scaling factors computed from the numerical simulation with the theoretical ones described in Section 2.1. The comparison shows that the numerical and theoretical normalized scaling factors match well.

Next, Fig. 5 compares the S_0 and A_0 modes decomposed by the proposed technique with the ones individually excited by the collocated PZTs A and C as shown in Fig. 3. Here, the theoretical normalized scaling factors were used for the proposed mode decomposition technique. In the first column, the decomposed S_0 mode signal (the dashed line) is compared with the corresponding S_0 mode signal (the solid line) generated by exciting the collocated PZTs A and C in-phase. Similarly, the decomposed A_0 signal is compared with the corresponding A_0 mode signal selected generated by exciting the collocated PZTs A and C out-of-phase. Due to limited space, the decomposition results obtained from only V_{13} and V_{23} are shown in Fig. 5. The proposed technique successfully decomposes the S_0 and A_0 modes from V_{ij} so that the decomposed S_0 and A_0 modes match well with the selectively generated S_0 and A_0 modes using the collocated PZTs. It can be also seen that the reflections of the S_0 and A_0 modes as well as their first arrivals are effectively decomposed.

Finally, the numerical example in Fig. 6 is presented to justify the use of multiple signals in solving the over-determined system in Eq. (8). In Fig. 6(a) and (b), all scaling factors in Eq. (8) are used for mode decomposition. On the other hand, in Fig. 6(c) and (d), a 2-by-2 scaling factor matrix composed of only S_{22}, A_{22}, S_{33} and A_{33} is used for mode decomposition. Comparisons of decomposed signals using 9×2 and 2×2 normalized scaling factor matrices demonstrate how the use of multiple signals can improve the decomposition performance.
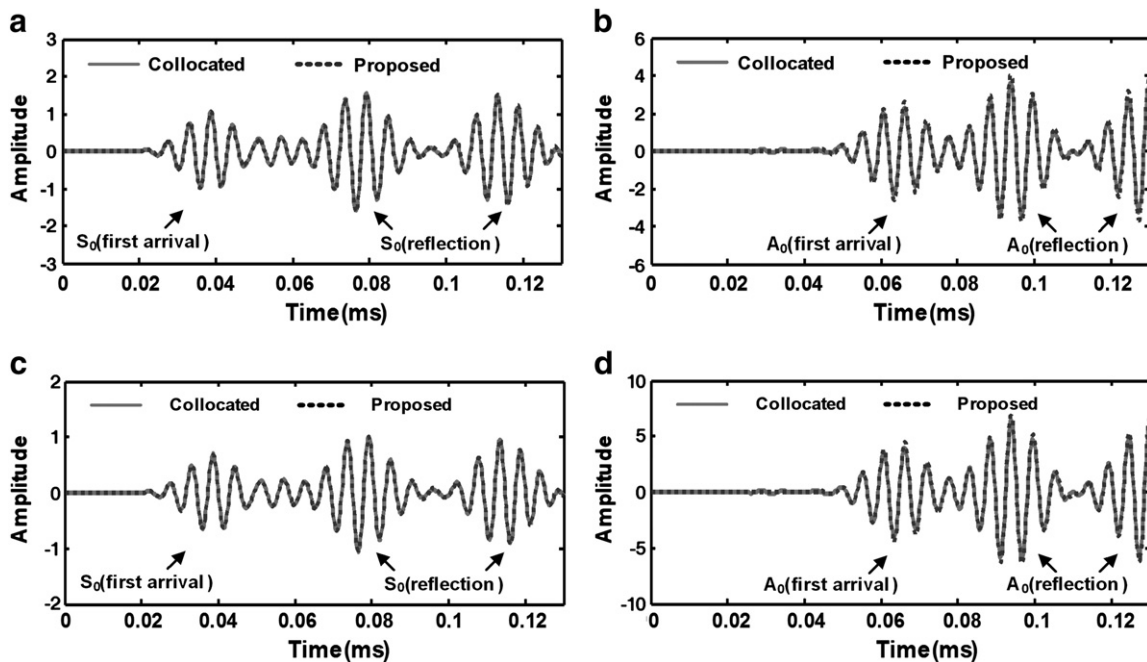

Fig. 5. Comparison between the S_0 and A_0 modes decomposed by the proposed technique (the dashed line) and the ones selectively generated by the collocated PZTs A and C in Fig. 3 (the solid line): (a) the S_0 modes in V_{13}, (b) the A_0 modes in V_{13}, (c) the S_0 modes in V_{23}, and (d) the A_0 modes in V_{23}.
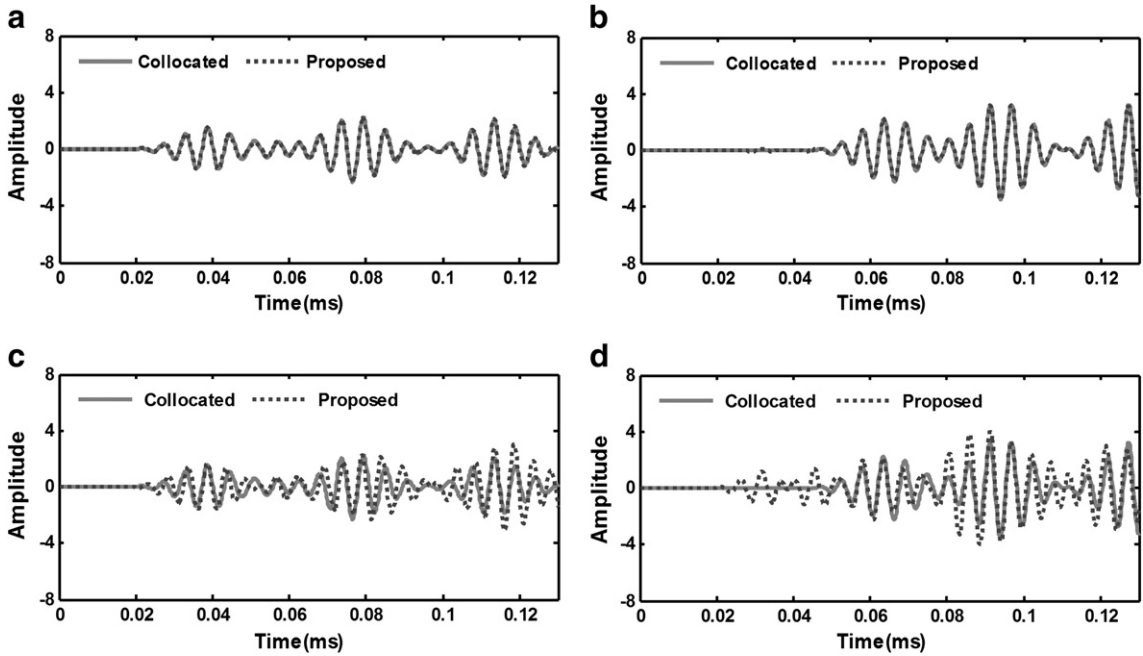
Fig. 6. The usefulness of using an over-determined normalized scaling factor matrix: it has been numerically demonstrated that the decomposition performance can be improved by using a 9×2 normalized scaling factor matrix rather than a 2×2 matrix. (a) the S_0 modes in V_{22} decomposed using a 9×2 scaling factor matrix, (b) the A_0 modes in V_{22} decomposed using a 9×2 scaling factor matrix, (c) the S_0 modes in V_{22} decomposed using a 2×2 scaling factor matrix and (d) the A_0 modes in V_{22} decomposed using a 2×2 scaling factor matrix. (The dashed line and solid line are obtained by the proposed technique and the collocated PZTs A and C in Fig. 3, respectively.)

4. Test results

4.1. Experimental setup

To further examine the feasibility of the proposed technique, experiments have been conducted on an aluminum plate. The dimension of the aluminum plate used in this study was 1000 mm × 1000 mm × 3 mm and three identical dual PZTs were placed on the top of the plate and another identical dual PZT is placed on the other side of the plate shown in Fig. 7. PZTs A and C are located at an identical position but attached on the different side. Note that PZT C is only used for the validation of the proposed technique and not needed for its actual implementation. Based on the theoretical velocities of the S_0 and A_0 modes at the driving frequency, the spacing between PZTs A and D was determined so that the first arriving S_0 mode is separated from the first arriving
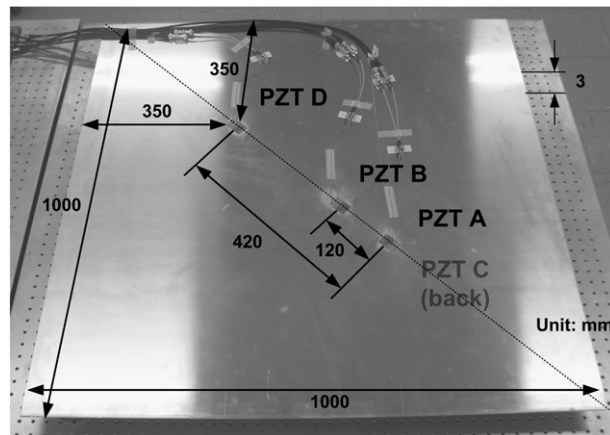

Fig. 7. The configuration and dimension of the test specimen including four identical dual PZTs: PZTs A, B and D were installed on the top side of the plate and PZT C was located at the same position with PZT A but on the other side of the plate.
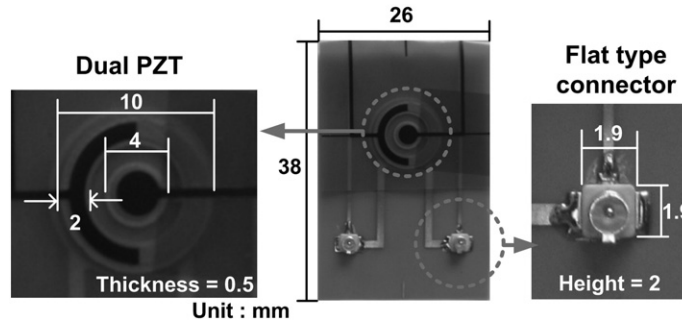
Fig. 8. The dimension of the newly designed dual PZT with flat type connectors used in this study.

A_0 mode. On the other hand, PZT B was placed closer to PZT A so the S_0 and A_0 modes overlap. The dual PZT used in this study was composed of circular and ring parts shown in Fig. 8. In order to electrically isolate the dual PZT from the host structure and make wire connections to the dual PZTs easier, the dual PZTs are packaged with Kapton films [25].

The data acquisition system consists of an arbitrary waveform generator (AWG), a high speed signals digitizer (DIG), a low noise preamplifier (LNP), a power amplifier and multiplexers. Using the 14-bit AWG, a toneburst signal with a 12 peak-to-peak voltage and a driving frequency of 180 kHz was generated and applied. The driving frequency was selected to generate the S_0 and A_0 modes with similar amplitudes. The output voltage was filtered and amplified 50 times by the LNP, and measured by the DIG of which sampling rate and resolution were 20 ms/s and 16 bits, respectively. The response signals were measured twenty times and averaged in the time domain to improve the signal-to-noise ratio.

4.2. Experimental results

First, the effectiveness of the proposed technique is investigated using the path AD which has a longer spacing between the excitation and sensing PZTs. Fig. 9 shows V_{ij} measured from the path AD where the first arriving S_0 and A_0 modes are well separated. Here, the first three wave packets indicate the first arriving S_0 and A_0 and reflected S_0 modes from plate boundaries, respectively. As expected, the S_0 and A_0 modes in V_{11}, V_{23} and V_{33} have an identical arrival time but different amplitudes.

Once the normalized scaling factors are computed from the signed amplitudes of the first arriving S_0 and A_0 modes included in V_{ij}, the S_0 and A_0 modes are decomposed by following the procedure described in Section 2.3. Fig. 10 compares the S_0 and A_0 modes in the path AD decomposed by the proposed technique (the dashed line) with the S_0 and A_0 modes selectively excited (the solid line) by the collocated PZTs A and C as shown in Fig. 7. For the generation of the S_0 and A_0 modes, collocated PZTs A and C were excited in-phase and out-of-phase, respectively. The test results show that the first arrivals and/or reflections of the S_0 and A_0 modes decomposed by the proposed technique well agree with the selectively generated ones.

Fig. 11 shows that the normalized scaling factors in the path AD were in good agreement with those in the path AB where the first arriving S_0 and A_0 modes overlap. In theory, the normalized scaling factors should be identical among these two paths as long as the sizes of the used dual PZTs are identical. Thus, the S_0 and A_0 modes in the path AB can be decomposed using the normalized scaling factors obtained from the path AD even if the amplitudes of the S_0 and A_0 modes cannot be obtained from the path AB. Note that the normalized scaling factors in the AB path shown in Fig. 11 were calculated from the amplitudes of the selectively generated S_0 and A_0 modes using collocated PZTs A and C. These normalized scaling factors from the collocated PZTs are used only for the comparison of the normalized scaling factors from the paths AD and AB. The actual mode decomposition of signals in the path AB is accomplished using the normalized scaling factors estimated from the path AD.

Fig. 12 shows the S_0 and A_0 modes at the path AB decomposed using the normalized scaling factors estimated from the path AD. The result shows that the decomposed S_0 and A_0 modes are in a good agreement with the selectively generated S_0 and A_0 modes signals. Even the first and/or second reflections of the S_0 and A_0 modes can be effectively extracted from the measured signals.
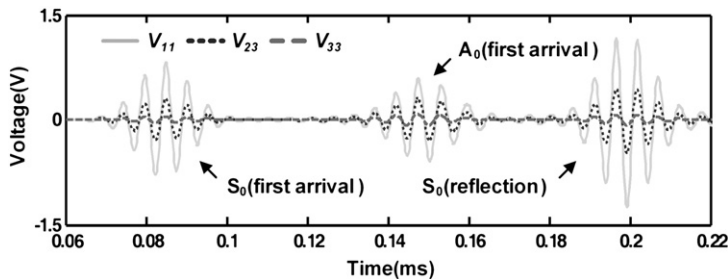

Fig. 9. Comparison of V_{11}, V_{23} and V_{33} measured from the path AD: the S_0 and A_0 modes included in different V_{ij}s have an identical arrival time but different amplitudes. (Due to limited space, only V_{11}, V_{23} and V_{33} out of nine V_{ij}s are plotted.)
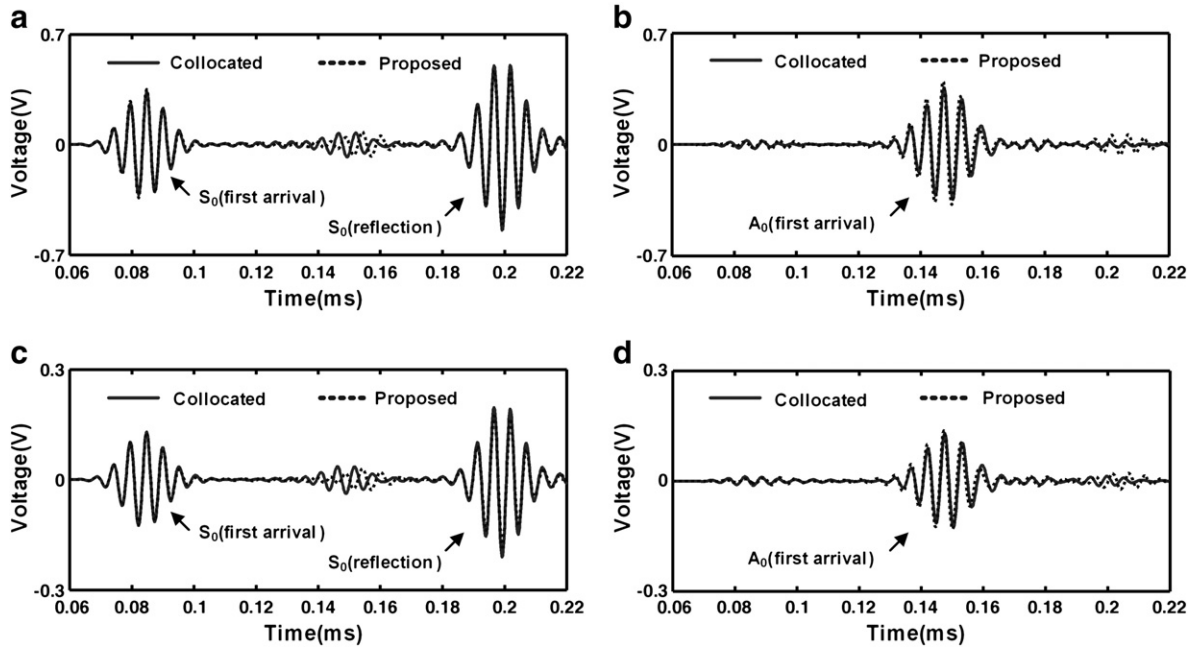
Fig. 10. Comparison between the S_0 and A_0 modes in the path AD decomposed by the proposed technique (the dashed line) and the ones selectively generated by the collocated PZTs A and C in Fig. 6 (the solid line): (a) the S_0 modes in V_{13}, (b) the A_0 modes in V_{13}, (c) the S_0 modes in V_{32} and (d) the A_0 modes in V_{32}.

In Figs. 10 and 12, the errors in the "proposed" case are mainly due to the size difference between the ring and the circular sensing PZTs. The use of this narrowband excitation rather than the single frequency excitation produces "spreading error" as described in Section 2.5. On the other hand, the errors in the "collocated" case are mainly caused by the bonding condition difference between the top and bottom PZTs. It is noted that the proposed technique achieves a mode decomposition performance comparative to the one obtained by the collocated PZTs.

5. Conclusion

In this study, a new Lamb wave decomposition technique is developed so that fundamental Lamb wave (S_0 and A_0) modes can be extracted from Lamb wave signals excited and measured by a pair of dual PZTs. The newly designed dual PZT consists of co-centered ring and circular PZTs, and multiple Lamb wave signals in a single wave path are generated and measured by activating different parts of the dual PZTs. Then, the mode decomposition is achieved through manipulating these multiple signals obtained from a pair of dual PZTs. The main advantage of the proposed decomposition technique is that both S_0 and A_0 modes can be decomposed at any desired frequency without any other special tuning such as the adjustment of the PZT size. Numerical simulation and experimental tests were conducted to validate the effectiveness of the proposed Lamb wave decomposition technique. Furthermore, since the scaling factors, necessary for the proposed decomposition technique can be instantaneously estimated from the target path or a reference path nearby, the proposed technique is expected to be less sensitive to changing
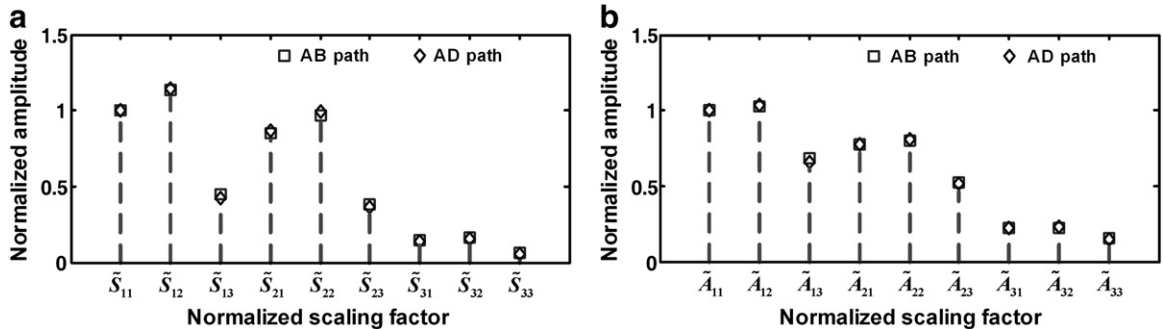

Fig. 11. Comparison of the normalized scaling factors of the S_0 and A_0 modes obtained from the paths AB and AD: (a) the S_0 mode and (b) the A_0 mode. (The rectangle and the diamond indicate the normalized scaling factors from the paths AB and AD.)
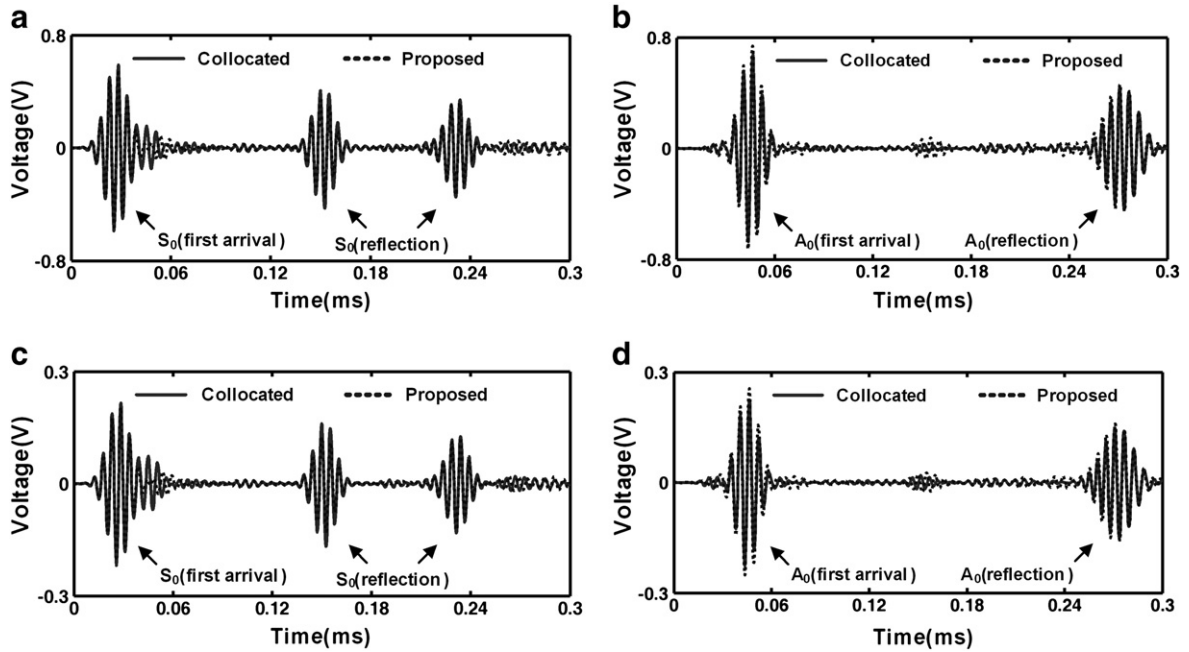
Fig. 12. Comparison between the S_0 and A_0 modes in the path AB decomposed by the proposed technique (the dashed line) and the ones selectively generated by the collocated PZTs A and C in Fig. 6 (the solid line): (a) the S_0 modes in V_{13}, (b) the A_0 modes in V_{13}, (c) the S_0 modes in V_{32} and (d) the A_0 modes in V_{32}.

temperature conditions. However, it should be noted that the proposed technique best operates under the following assumptions: (1) the target structure has a uniform thickness and isotropic material properties; (2) all the dual PZTs installed are identical in terms of their sizes and bonding conditions; (3) the driving frequency is selected so that only the S_0 and A_0 modes are excited; and (4) spatial distribution of temperature over the specimen is uniform although temperature variation over time is allowed and has no effect on the proposed technique. A further study is underway to extend the proposed concept to anisotropic structures and complex geometries with stiffeners or welded joints.

Acknowledgements

Appendix A. Integral of the Lamb wave response over a circular PZT area

Fig. A1 shows the circular excitation PZT positioned at the origin and the other sensing PZT centered at $(r_s,0)$. The dotted circle represents the equal strain field generated from the edge of the excitation PZT. The output voltage of the sensing PZT can be obtained by integrating the strain field over the entire sensing area and by multiplying it with the constants shown in Eq. (3). This integration can be simplified by assuming that (1) the distance between the excitation and sensing PZTs
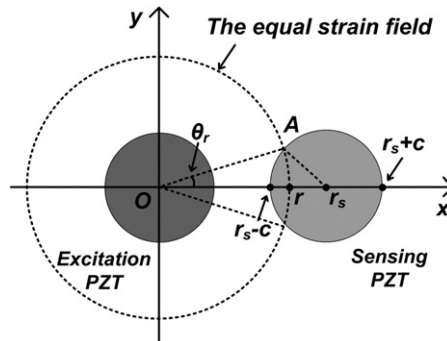

Fig. A1. The response calculation of a circular sensing PZT with the center at $(r_s,0)$ and radius c when Lamb waves are generated by a circular excitation PZT with a radius r at the origin of the coordinate. The dash line represents the equal strain field generated by the circular excitation PZT.

is much longer compared to the size of the sensing PZT and (2) the complex Hankel function shows an asymptotic behavior after four or five cycles of the wavelength of the excited mode [21].

First, θ_r in Fig. A1 is represented as a function of c, r_s and r. In Fig. A1, point A is one of the intersections between the circular equal strain field (dotted circle) with a radius of r and the edge of the circular sensing PZT with a radius of c. θ_r is an angle between OA and x-axis. When the radius of the sensor (c) is small enough compared to the wave propagation distance (r), the higher order terms of the Maclaurin series of $\cos \theta_r$ can be omitted and $\cos \theta_r \cong 1 - \theta_r^2/2$. Then, θ_r becomes:

$$\theta_r = \sqrt{\frac{c^2 - (r_s - r)^2}{r_s r}} \tag{A1}$$

Next, the Hankel function can be approximated as follows using the fact that it exhibits an asymptotic behavior after four or five cycles of the wavelength of the mode considered [21]:

$$H_0^{(2)}(\xi r) \cong \sqrt{\frac{2}{\pi \xi r}} e^{i(\xi r - \frac{\pi}{4})} \tag{A2}$$

By submitting Eqs. (A1) and (A2) into Eq. (4), the output voltage becomes:

$$V(t) = -i \frac{2\tau_0 E_s h_s g_{31} a}{\mu c^2} \sqrt{\frac{2}{\pi r_s}} e^{i(\omega t - \frac{\pi}{4})} \cdot$$
$$\left[J_1(\xi^{S_0} a) \frac{N_S(\xi^{S_0})}{D'_S(\xi^{S_0})} \int_{r_s - c}^{r_s + c} \sqrt{\xi^{S_0} \{c^2 - (r_s - r)^2\}} e^{i\xi^{S_0} r} dr + J_1(\xi^{A_0} a) \frac{N_A(\xi^{A_0})}{D_A(\xi^{A_0})} \int_{r_s - c}^{r_s + c} \sqrt{\xi^{A_0} \{c^2 - (r_s - r)^2\}} e^{i\xi^{A_0} r} dr \right]. \tag{A3}$$

Note that only the fundamental symmetric (S_0) and antisymmetric (A_0) modes are included in Eq. (A3) without loss of generality.

Eq. (A3) can be further simplified using the Poisson integral of the Bessel function [23]

$$J_n(z) = \left(\Gamma\left(n + \frac{1}{2}\right) \Gamma\left(\frac{1}{2}\right) \right)^{-1} \left(\frac{1}{2} z\right)^n \int_{-1}^{+1} \left(1 - t^2\right)^{n - \frac{1}{2}} e^{izt} dt \tag{A4}$$

where $\Gamma()$ is the Gamma function. Finally, the output voltage of the circular sensing PZT with a radius of c corresponding to the other circular PZT excitation with a radius of a becomes:

$$V(t) = -i \frac{2\tau_0 E_s h_s g_{31} a}{\mu c} \sqrt{\frac{2\pi}{r_s}} \left[\begin{array}{l} \frac{1}{\sqrt{\xi^{S_0}}} J_1(\xi^{S_0} a) J_1(\xi^{S_0} c) \frac{N_S(\xi^{S_0})}{D'_S(\xi^{S_0})} e^{i(\omega t - \frac{\pi}{4} + \xi^{S_0} r_s)} \\ + \frac{1}{\sqrt{\xi^{A_0}}} J_1(\xi^{A_0} a) J_1(\xi^{A_0} c) \frac{N_S(\xi^{A_0})}{D'_S(\xi^{A_0})} e^{i(\omega t - \frac{\pi}{4} + \xi^{A_0} r_s)} \end{array} \right]. \tag{A5}$$

Appendix B. Calculation of the response model of a dual PZT

The radial displacement at a single point generated by a ring-shape PZT with outer and inner radii of a_1 and a_2 becomes [21]:

$$u_r(r, z = h) = -\pi i \frac{\tau_0}{\mu} e^{i\omega t} \cdot \left[\begin{array}{l} \sum_{\xi^S} \left(a_1 J_1(\xi^S a_1) - a_2 J_1(\xi^S a_2) \right) \frac{N_S(\xi^S)}{D'_S(\xi^S)} H_1^{(2)}(\xi^S r) \\ + \sum_{\xi^A} \left(a_1 J_1(\xi^A a_1) - a_2 J_1(\xi^A a_2) \right) \frac{N_A(\xi^A)}{D'_A(\xi^A)} H_1^{(2)}(\xi^A r) \end{array} \right] \tag{B1}$$

where N_S (N_A) and D_S (D_A) are defined in Section 2.1. Basically, the response model generated by the ring PZT can be obtained by subtracting the response corresponding to the inner circle PZT with a radius of a_2 from that corresponding to the outer circular PZT with a radius of a_1.

The output voltage response at the ring sensing PZT can be obtained by integrating the surface strain in Eq. (2) over the ring-shape of the sensing PZT. Similar to the ring-shape excitation, the response of the ring-shape PZT is calculated by subtracting the strain over the inner circular area from the strain of the outer circular area.

Next, the relationships among various S_{ij}s and A_{ij}s can be obtained using the following two superposition relationships. In the first superposition relationship, the summation of the response signals obtained by the individual excitations of the ring and circular PZTs is equal to the response obtained by the excitation of the entire PZT area for any fixed sensing PZT size:

$$V_{1j} = V_{2j} + V_{3j} \quad \text{for } j = 1\text{~}3. \tag{B2}$$

The other superposition relationship is established for the varying sensing PZT size. The output voltage obtained by the entire area of the dual PZT is the weight summation of the responses separately measured by the ring and the circular PZTs, and the weight values are determined by the relative areas of the corresponding sensing PZT parts:

$$V_{i1} = \alpha V_{i2} + \beta V_{i3} \quad \text{for } i = 1\text{~}3 \tag{B3}$$

where $\alpha + \beta = 1$, and α and β are the ratios of the ring and the circular PZT areas to the entire PZT area.

Based on Eq. (B1) and two superposition relationships in Eqs. (B2) and (B3), all nine signals (V_{ij} for $i, j = 1$, 2 and 3) can be obtained as follow:

$$\mathbf{V} = \mathbf{S}\mathbf{C} \tag{B4}$$

where a_1, a_2 and a_3 are the outer and the inner radii of the ring PZT and the radius of the inner circular PZT, respectively,

$$\mathbf{V} = \begin{bmatrix} V_{11} \\ V_{12} \\ \vdots \\ V_{33} \end{bmatrix}, \mathbf{S} = \begin{bmatrix} S_{11} & A_{11} \\ S_{12} & A_{12} \\ \vdots & \vdots \\ S_{33} & A_{33} \end{bmatrix}, \mathbf{C} = \begin{bmatrix} C^{S_0}(t, r_s) \\ C^{A_0}(t, r_s) \end{bmatrix}$$

$$S_{33} = S^{S_0}(a_3, a_3)$$

$$S_{23} = S^{S_0}(a_1, a_3) - S^{S_0}(a_2, a_3)$$

$$S_{32} = (K_1 - K_2)^{-1} \left(K_1 S^{S_0}(a_3, a_1) - K_2 S^{S_0}(a_3, a_2) \right),$$

$$S_{22} = (K_1 - K_2)^{-1} \begin{bmatrix} K_1 \left(S^{S_0}(a_1, a_1) - S^{S_0}(a_3, a_1) \right) \\ -K_2 \left(S^{S_0}(a_1, a_2) - S^{S_0}(a_3, a_2) \right) \end{bmatrix},$$

$$S_{21} = (K_1 - K_2 + K_3)^{-1} \{ (K_1 - K_2) S_{22} + K_3 S_{23} \},$$

$$S_{31} = (K_1 - K_2 + K_3)^{-1} \{ (K_1 - K_2) S_{32} + K_3 S_{33} \},$$

$$S_{13} = S_{23} + S_{33}, S_{12} = S_{22} + S_{32}, S_{11} = S_{21} + S_{31},$$

$$K_j = \pi \left(a_j \right)^2,$$

A_{ij} are defined in a similar fashion using $S^{A_0}(a_i, a_j)$, $C^{A_0}(t, r_s)$ and K_j.

References

[1] D. Alleyne, P. Cawley, The interaction of Lamb waves with defects, IEEE Trans. Ultrason. Ferroelectr. Freq. Control 39 (1992) 381–397.
[2] A. Raghavan, C.E.S. Cesnik, Review of guided-wave structural health monitoring, Shock Vib. Dig. 39 (2007) 91–114.
[3] S.S. Kessler, S.M. Spearing, C. Soutis, Damage detection in composite materials using Lamb wave methods, Smart Mater. Struct. 11 (2002) 269–278.
[4] Z. Su, L. Ye, Y. Lu, Guided Lamb waves for identification of damage in composite structures: a review, J. Sound Vib. 295 (2006) 753–780.
[5] V. Giurgiutiu, Structural Health Monitoring: with Piezoelectric Wafer Active Sensors, Academic Press, San Diego, CA, 2008, pp. 309–362.
[6] H. Sohn, S.B. Kim, Development of dual PZT transducers for reference-free crack detection in thin plate structures, IEEE Trans. Ultrason. Ferroelectr. Freq. Control 57 (2010) 229–240.
[7] F.L. di Scalea, H. Matt, I. Bartoli, The response of rectangular piezoelectric sensors to Rayleigh and Lamb ultrasonic waves, J. Acoust. Soc. Am. 121 (2007) 175–187.
[8] S.R. Anton, D.J. Inman, G. Park, Reference-free damage detection using instantaneous baseline measurements, AIAA J. 47 (2009) 1952–1964.
[9] S.B. Kim, H. Sohn, Instantaneous reference-free crack detection based on polarization characteristics of piezoelectric materials, Smart Mater. Struct. 16 (2007) 2375–2387.
[10] J.B. Ihn, F.K. Chang, Detection and monitoring of hidden fatigue crack growth using a built-in piezoelectric sensor/actuator network: I. diagnostics, Smart Mater. Struct. 13 (2004) 609–620.
[11] P.D. Wilcox, M.J.S. Lowe, P. Cawley, Mode and transducer selection for long range Lamb wave inspection, J. Intell. Mater. Syst. Struct. 12 (2001) 553–565.
[12] M. Castaings, P. Cawley, The generation, propagation, and detection of Lamb waves in plates using air-coupled ultrasonic transducers, J. Acoust. Soc. Am. 100 (1996) 33070–33077.
[13] I.A. Viktorov, Rayleigh and Lamb Waves, Plenum, New York, 1967, pp. 67–83.
[14] J.L. Rose, S.P. Pelts, M.J. Quarry, A comb transducer for mode control in guided wave NDE, IEEE Ultras. Symp. Proc. (1996) 857–860.
[15] F.L. Degertekin, B.T. Khuri-Yakub, Single mode lamb wave excitation in thin plates by Hertzian contacts, Appl. Phys. Lett. 69 (1996) 146–148.
[16] K. Yamanaka, Y. Nagat, T. Koda, Selective excitation of single-mode acoustic waves by phase velocity scanning of a laser beam, Appl. Phys. Lett. 58 (1991) 1591–1593.
[17] Z. Su, L. Ye, Selective generation of Lamb wave modes and their propagation characteristics in defective composite laminates, J. Mater: Des. Appl. (2004) 95–110.
[18] S.C. Wooh, Y.J. Shi, Synthetic phase tuning of guided waves, IEEE Trans. Ultrason. Ferroelectr. Freq. Control 48 (2001) 209–223.
[19] F.L. di Scalea, H. Matt, I. Bartoli, The response of rectangular piezoelectric sensors to Raleigh and Lamb ultrasonic waves, J. Acoust. Soc. Am. 121 (2007) 175–187.
[20] G.B. Santoni, L. Yu, B. Xu, V. Giurgiutiu, Lamb wave-mode tuning of piezoelectric wafer active sensors for structural health monitoring, J. Vib. Acoust. 129 (2007) 752–762.
[21] A. Raghavan, C.E.S. Cesnik, Finite-dimensional piezoelectric transducer modeling for guided wave based structural health monitoring, Smart Mater. Struct. 14 (2005) 1448–1461.
[22] H. Sohn, S.J. Lee, Lamb wave tuning curve calibration for surface-bonded piezoelectric transducers, Smart Mater. Struct. 19 (2010) 015007.
[23] G.N. Watson, A Treatise on the Theory of Bessel Functions, 2nd ed., Cambridge U. P, London, 1958, pp. 24–26.
[24] S.S. Kessler, D.J. Shim, Validation of a Lamb wave-based structural health monitoring system for aircraft applications, Proc. SPIE Smart Structures/NDE Joint Conference, San Diego, CA, 2005, pp. 293–301.
[25] http://www.metisdesign.com, (date last viewed 4/21/10).